

Effect of oxygen isotope substitution and crystal micro-structure on magnetic ordering and phase separation in

$$(\text{La}_{1-y}\text{Pr}_y)_{0.7}\text{Ca}_{0.3}\text{MnO}_3$$

V. Yu. Pomjakushin and D. V. Sheptyakov

Laboratory for Neutron Scattering, ETHZ & PSI, CH-5232 Villigen PSI, Switzerland

K. Conder

*Laboratory for Developments and Methods,
PSI, CH-5232 Villigen PSI, Switzerland*

E. V. Pomjakushina

*Laboratory for Developments and Methods,
PSI, CH-5232 Villigen PSI, Switzerland and
Laboratory for Neutron Scattering, ETHZ & PSI, CH-5232 Villigen PSI, Switzerland*

A. M. Balagurov

Frank Laboratory of Neutron Physics, JINR, 141980, Dubna, Russia

(Dated: October 10, 2018)

Abstract

The crystal and magnetic structures of the specified CMR manganite system have been studied as a function of $y = (0.2 - 1)$ across the metal-insulator (MI) transition, and of the oxygen mass (^{16}O , ^{18}O). We quantitatively show how the polaronic narrowing of the carrier bandwidth and the crystal lattice micro-strains control the volume fractions of the mesoscopic ferro- and antiferromagnetic clusters. A well-defined dip in the transition temperatures and the suppression of all the types of long range ordering seen near the MI-transition at $y \simeq 0.9$ indicate a key role of the quenched disorder for the formation of the long-scale phase separated state.

PACS numbers: 75.47.Gk, 61.12.Ld, 75.30.-m,

I. INTRODUCTION

The presence of large¹ or giant oxygen isotope effects^{2,3} in the colossal magnetoresistance (CMR) manganese oxides $A_{1-x}A'_x\text{MnO}_3$ (A is rare earth element, A' is Ca, Sr, Ba) is now well established and it is proven to be an intrinsic property of these systems. Due to the strong electron-phonon coupling mediated by the Jahn-Teller effect the substitution of ^{16}O by ^{18}O can significantly change the effective exchange interaction between neighboring Mn ions⁴. In case of double exchange (DE) type of interaction the increase in the oxygen mass strongly reduces the effective charge carrier bandwidth, thus shifting the system towards insulating state, while the standard superexchange with large Hubbard energy gap is not supposed to be affected by the oxygen mass. Thus the value of the isotope effect on the metallic and insulating states of the above systems can reveal the underlying interatomic and electron lattice interactions responsible for particular magnetic, charge and orbital ordering, which are strongly coupled together because of the 3d-electron anisotropy and the mixed $\text{Mn}^{3+}/\text{Mn}^{4+}$ valence. The low bandwidth manganite family $(\text{La}_{1-y}\text{Pr}_y)_{0.7}\text{Ca}_{0.3}\text{MnO}_3$ (LPCM hereafter) has the fixed optimal hole doping $x = 0.3$ and variable A-cation radius $\langle r_A \rangle$ that is linearly connected with the Pr-concentration y . The principal effect of decreasing $\langle r_A \rangle$ is a decrease in Mn-O-Mn bond angle, which leads to the decrease in the electron transfer integral between the Mn-ions. The metal-insulator (M-I) boundary lays at the Pr-concentration between $y = 0.86$ and $y = 1.0$ ^{5,6}. The metallic state is conditioned by the well known double exchange and it is ferromagnetic (FMM), e.g. for $y = 0$ ^{7,8}. The magnetic structure of the insulating state can be both antiferromagnetic (AFMI) with the pseudo-CE type magnetic structure^{9,10} and ferromagnetic for the Pr-concentrations close to $y = 1$. The AFMI state is a Mott insulator state with the charge ordering of the $\text{Mn}^{3+}/\text{Mn}^{4+}$ ions similar to the case of $\text{La}_{0.5}\text{Ca}_{0.5}\text{MnO}_3$, whereas the origin of the genuine ferromagnetic insulating phase (FMI) is not completely understood and it is characterized by a non-ordinary kind of orbital/charge ordering^{11,12,13,14}. The LPCM system can be converted from the metallic to insulating state by the isotope substitution^{3,15}. Similar giant isotope effect was observed in $(\text{La}_{0.5}\text{Nd}_{0.5})_{0.67}\text{Ca}_{0.33}\text{MnO}_3$ ². The complete suppression of the ferromagnetic transition temperature cannot be attributed to a solely polaronic narrowing of the bandwidth within the DE model^{1,4}, but requires an inhomogeneous phase separated state, which was indeed directly observed by different experimental techniques in $(\text{La}_{1-y}\text{Pr}_y)_{0.7}\text{Ca}_{0.3}\text{MnO}_3$ ^{10,16}

and in the similar series $\text{La}_{5/8-y}\text{Pr}_y\text{Ca}_{3/8}\text{MnO}_3$ ^{17,18}. The neutron diffraction study¹⁵ has shown that the increase in the oxygen mass completely converts the dominating FMM metallic phase into the insulating charge ordered AFMI one in LPCM with $y = 0.75$. The presence of the long scale percolate phase separation in the manganites itself has been attracting special experimental and theoretical attention. There are two main concepts of the mesoscopically inhomogeneous state in the manganites. One standpoint is that the intrinsic quenched disorder enhances the fluctuations of the competing orders near the original bi-critical point^{19,20,21,22,23,24}. In another approach, the lattice distortions and the long-range strain^{18,25,26,27} are the dominant factors controlling the phase separation, similar to the one observed at the martensite type structural transition. Motivated by the spectacular giant isotope effect and the problem of phase separation we have undertaken a systematic neutron and synchrotron x-ray diffraction study of a series of the samples $(\text{La}_{1-y}\text{Pr}_y)_{0.7}\text{Ca}_{0.3}\text{MnO}_3$ for $y = 0.2 - 1.0$ with ^{16}O and ^{18}O . In the paper we present the detailed data on the structure and magnetic properties of the FMM, FMI and the charge ordered AFMI phases and discuss the key parameters conditioning the giant isotope effect and the phase separation in the LPCM-system. Earlier we have performed a diffraction study with another series of samples of the same system prepared by a different chemical route¹⁰, in which the effect of the oxygen isotope substitution has been studied only for one concentration $y = 0.75$. Moreover the different synthesis route used in the present study gives different microstructure parameters, which as we show below, have influence on the phase separation and hence on the oxygen substitution effect.

The paper is organized as follows. In Sec. II the details of the sample synthesis, oxygen treatment and the experimental measurements are given. In Sec. III A the temperature dependences of the magnetic susceptibility $\chi(T)$ are analyzed. The ferromagnetic transition temperatures T_C determined from $\chi(T)$ are used as independent estimations of T_C complementary to ones determined from the neutron diffraction measurements. In Sec. III B the room temperature crystal structure and microstructure parameters as a function of y are compared for ^{16}O and ^{18}O -samples. In Sec. III C the structure parameters are analyzed as a function of temperature between 15 K and 1200 K across the orbital order-disorder transition at $\simeq 700$ K. In Sec. III D we show the evolution of the orbital and charge order as a function of doping y . In Sec. III E the data on the temperature dependence of the magnetic state and the spatial phase separation are presented. The magnetic transition temperatures and

the magnetic ground state (the phase fractions, ordered magnetic moments) are obtained as a function of doping y and the oxygen mass. Sec. III F explains the connection between the phase separation and the lattice micro-strains (static variance of metric parameters). In Sec. III G the suppression of all types of ordering near critical concentration $y_c = 0.9$ is discussed. This effect can be well interpreted in the theoretical model^{19,20}, which assumes the presence of competing states and quenched disorder near y_c .

II. SAMPLES. EXPERIMENTAL

The crystal structure parameters of a LPCM sample for given y depend not only on y but also on the sample preparation procedure. For example, the spontaneous orthorhombic strain, thermal displacement parameters (reflecting also the local static disorder), the lattice micro-strains decrease as a function of annealing time and of the cooling time through the high temperature pseudocubic-orthorhombic structural transition. Thus, a precise study of a real LPCM system as a function of y and the oxygen mass can be done only within a series of samples prepared and thermally treated at the very identical conditions. The samples, which are denoted as “O-series”, were calcined at temperatures 1270-1570 K for 100h from La_2O_3 , Pr_6O_{11} , MnO_2 oxides and CaCO_3 with 3 intermediate grindings. These samples we call “as-prepared”. The final ^{18}O - and ^{16}O -samples were obtained via respective oxygen isotope exchange in closed quartz tubes in parallel under the controlled gas pressure slightly above 1 bar at 1270 K during 40h and then cooled down to 290 K with the rate 30 K/h. The ^{18}O -samples had 80% of ^{18}O -isotope, measured by the weight gain after the oxygen exchange. The control weighing of the ^{16}O -sample gave the same mass within accuracy 0.03%. The mass of each sample was about 2 g. The oxygen content in all the samples was determined by the thermogravimetric hydrogen reduction²⁸ and amounted to 3.003(5). The samples with $y = 0.85$ and 0.95 were prepared only with ^{16}O . One of the samples which has been studied earlier^{10,15,29}, was also oxygen treated in the same way as all the samples from the O-series. This sample is from a series prepared by a synthesis from the aqueous solutions of the respective metals nitrates (denoted as “N-series”).

The *ac* magnetic susceptibility $\chi(T) = \chi'(T) + i\chi''(T)$ was measured in zero external field with amplitude of the *ac* field 10 Oe and frequency 1 kHz using Quantum Design PPMS station. Neutron powder diffraction experiments were carried out at the SINQ spallation

source of Paul Scherrer Institute (Switzerland) using the high-resolution diffractometer for thermal neutrons HRPT³⁰ ($\lambda = 1.866, 1.494$ Å, high intensity mode $\Delta d/d \geq 1.8 \cdot 10^{-3}$), and the DMC diffractometer³¹ situated at a supermirror coated guide for cold neutrons at SINQ ($\lambda = 2.56$ Å). All the temperature scans were carried out on heating. X-ray synchrotron diffraction at room temperature was done at the Material Sciences beam line (MS, SLS/PSI). The refinements of the crystal and magnetic structure parameters were carried out with FULLPROF³² program, with the use of its internal tables for scattering lengths and magnetic form factors.

III. RESULTS AND DISCUSSION

A. Magnetic susceptibility

The main use of the magnetic susceptibility data $\chi(T)$ for the purposes of the present work is the determination of the ferromagnetic transition temperatures, complementary to the NPD data. The $\chi(T)$ as a function of temperature is shown in Fig. 1 for several selected samples [since the $\chi(T)$ are quite similar for the samples with close values of Pr-concentrations, not all the $\chi(T)$ -curves are shown to avoid the plot overload]. This plot nicely illustrates the systematic decrease in the magnetic transition temperatures as a function of the oxygen mass. All the samples show (Fig. 2) the ferromagnetic type of the Curie-Weiss susceptibility $\chi'(T)$ at high temperatures. The slope of the $\chi'^{-1}(T)$ becomes non-linear below 250 K due to the presence of the antiferromagnetic correlations which are developed as the temperature decreases down to the Néel temperature $T_N \simeq 150$ K. The Curie-Weiss temperatures T_{CW} were determined from the fit of the high temperature susceptibility to $\chi'(T) = C/(T - T_{CW})$ in the temperature range (270 – 335 K) depending on y content. The Curie-Weiss temperatures amounted to $T_{CW} = 165 - 240$ K for the ^{16}O -samples for $y = 1 - 0.2$. They are in agreement with the ferromagnetic transition temperatures T_C determined from NPD only for $y = 0.2$ and 0.5, while for the higher Pr-content T_{CW} is significantly higher than T_C . In the ^{18}O -substituted samples the T_{CW} is decreased similar to the change in T_C , implying smaller effective electron transfer integral which mediates the ferromagnetic coupling for the heavier oxygen ion. The Curie-Weiss constant $C = N_A 2S(S + 1)\mu_B/3k$ allows estimating the paramagnetic Mn-spin value S . The experimental values of

C amounted to $4.6 - 6$ emu/mol depending on the y -content that correspond to the effective spin $2S \simeq 5.2 - 6$, instead of the expected value of 3.7 for the given $\text{Mn}^{3+}/\text{Mn}^{4+}$ ratio. The enhanced value of the Curie-Weiss constant is a typical feature of the ferromagnetic manganite system and is attributed to the formation of the ferromagnetic clusters well above T_C ^{33,34}. The quantitative analysis of C as a function of y is difficult because the Curie-Weiss constant value depends on the temperature interval used for the fit and the large variation of the T_C . The imaginary part of the susceptibility shows a maximum at a temperature very close to T_C for all y (Fig. 1). The maximum is caused by the absorption due to the ferromagnetic domains formation with sufficiently short relaxation times $\tau \sim 1/(2\pi f)$ close to T_C , where f is the external field frequency. This maximum is asymmetric and can be very broad, so the temperature of the maximum cannot be used for quantitative estimation of the T_C . A good way of the evaluation of the ferromagnetic transition temperature is the analysis of the derivative of the magnetic susceptibility $d\chi'/dT(T)$ which has a well defined minimum as shown in the insert of Fig. 2. The temperature of the minimum T_{min} will be taken as an independent, complementary to the NPD data, estimation of T_C .

B. Crystal structure and microstructure

The crystal structure for all the compositions $y = 0.2 - 1.0$ at all temperatures is well refined in single phase in the orthorhombic space group $Pnma$ with the standard for these compounds structure model (see e.g.²⁹). In general, the low temperature state is spatially mesoscopically phase separated, but the lattice constants of the phases are too close to each other and the two phase refinement is not reliable. However, there are cases where the structure separation is explicitly visible, e.g. in the system $\text{R}_{0.5}\text{Sr}_{0.5}\text{MnO}_3$ ($\text{R} = \text{Sm}, \text{Td}, \text{Tb}$) the metrics of the phases are sufficiently different and both phases can be identified in the neutron diffraction experiment³⁵. The examples of the x-ray synchrotron diffraction pattern and the neutron diffraction pattern and their refinements are shown in Fig. 3 and Fig. 4, respectively. All the room temperature ($T = 290$ K) crystal structure parameters except for the thermal displacement parameter do not depend on the oxygen mass within the accuracy 0.2%. The lattice constants, which are determined with the best accuracy (Fig. 5(a)) are slightly systematically smaller for the ^{18}O -samples: for $y \leq 0.5$ the unit cell volume V is 0.2% smaller, for the $y > 0.5$ the volumes V match within 0.02%. The only structure parameter

which is noticeably and systematically changed by the oxygen isotope substitution is the thermal displacement parameter B . The oxygen thermal parameter is slightly decreased, while the Mn and A-cation ones are pronouncedly increased as a function of oxygen mass (Fig. 5(b,c)). These changes agree with the expected behavior of the $B \sim (k_B T) \overline{\omega^{-2}} / M$, where M is the atom mass, the ω^{-2} is averaged over the phonon density of states $Z(\omega)$ ³⁶. The parameter $\overline{\omega^{-2}}$ should increase as a function of an average atom mass provided that the elastic force constants are not changed. Hence the thermal parameters of Mn and A-cation should increase, while the oxygen B -value behavior cannot be simply predicted because both $\overline{\omega^{-2}}$ and M are changing. Figure 6 illustrates systematic distortion of the structure as a function of the Pr-concentration y . The Mn-O-Mn bond angles are systematically decreased conditioning the change from the metallic to insulating state at the concentration above ~ 0.85 . At the same time the orthorhombic strain r is substantially increased with the increase in y . The values of strain r for the “as-prepared” samples (also shown in the Fig. 6a) are significantly larger stressing the point that the systematic study of the present system as a function of y and the oxygen mass is only possible within a series of samples prepared and treated in identical way.

The microstructure of the samples was obtained from the analysis of the Bragg peak broadening (anisotropic in general) as a function of scattering angle (2θ) by the following procedure. The Bragg peaks were described by the pseudo-Voigt distribution function with the Gaussian (Γ_G) and Lorentzian (Γ_L) components. The total peak width Γ was calculated from the individual components using a 5th order polynomial approximation as described in Ref.³⁷ and implemented in the FULLPROF code³². The angular dependence of the peak width was approximated by the Cagliotti-type function $\Gamma_G(2\theta) = ((U \tan^2 \theta + \sigma_G^2) + V \tan \theta + W + \sigma_{1G} / \cos^2 \theta)^{(1/2)}$ and $\Gamma_L(2\theta) = (X \tan \theta + \sigma_L) + (Y + \sigma_{1L}) / \cos \theta$ for the Gaussian and Lorentzian components respectively. All the widths correspond to the full width at half-maximum (FWHM) and the angles are measured in radians. U , W , U and Y were fixed to the values given by the instrumental resolution function. $\sigma_G(2\theta)$ and $\sigma_L(2\theta)$ are the Rietveld refined Gaussian and Lorentzian components related to the sample micro-strains. σ_{1G} and σ_{1L} are the refined components related to the finite size broadening. The total widths both for the micro-strain ($\sigma(2\theta)$) and the finite size (σ_1) broadening were calculated from the individual Gaussian and Lorentzian refined components by means the above mentioned 5th-order polynomial approximation. The apparent sizes (L) are connected

with the broadening σ_1 by well-known Debay formula $\sigma_1 = \lambda/L$. The micro-strains or the static fluctuations of crystal lattice constants are determined from the variance of the metric parameters (A, B, C) of the reciprocal space. The square of the reciprocal distance $1/d$ for a Bragg reflection with Miller indices (hkl) for the orthorhombic singony reads $1/d^2 = M_{hkl} = Ah^2 + Bk^2 + Cl^2$. The variance of M_{hkl} is related to the widths of the diffraction peaks as $\sigma(2\theta) = \sigma(M_{hkl})/M_{hkl} \tan \theta$. General description of the anisotropic peak broadening is given in Ref.³⁸. In our case we consider the isotropic micro-strains $(\delta d_{st}/d)$, where d stands for a , b or c lattice constants, and an additional micro-strain along a -axis $(\delta d_{st}/d)_{[100]}$ that have the contributions to the reciprocal distance variance $\sigma(M_{hkl}) = 2(\delta d_{st}/d)M_{hkl}$ and $2(\delta d_{st}/d)_{[100]}Ah^2$, respectively. The presence of the anisotropic broadening is nicely illustrated by the two doublets shown in the insert of Fig. 3.

The sample related peak broadening is comparable with the resolution of neutron diffraction instrument HRPT, therefore we have performed a comparative ultra-high resolution synchrotron x-ray diffraction study of several samples at room temperature. The examples of the reduced sample related peak widths $\delta d/d = \Gamma_{\text{sample}}/\tan(\theta)$ as a function of scattering vector $q = 2\pi/d$ are shown in the insert of Fig. 4. The width Γ_{sample} includes the isotropic micro-strains and the finite size broadening components. One can see that the experimental broadening is dominated by the micro-strain effect, which gives a constant term to $\delta d/d(q)$, whereas the finite size effect gives a $\propto 1/q$ term. The apparent sizes L are larger than $2 \cdot 10^3$ Å giving a relatively small contribution to the broadening (assuming $1/L = 0$ increases the refined micro-strain values by less than 10%). The micro-strains refined from the neutron and synchrotron data agree within the statistical error bars. This implies that in spite of lower resolution of the neutron diffraction data ($\delta d/d \simeq 2 \cdot 10^{-4}$ and $\geq 1.8 \cdot 10^{-3}$ for the synchrotron x-ray and neutrons respectively) we can reliably extract the microstructure parameters from the NPD data. The lattice micro-strains allow us to characterize the amount of quenched disorder and the presence of the charge ordering as discussed in the following sections.

There are two transitions in $(\text{La}_{1-y}\text{Pr}_y)_{0.7}\text{Ca}_{0.3}\text{MnO}_3$ associated with the changes in the crystal structure. The first transition at high temperature is a first order isostructural phase transition from the pseudo-cubic to the orthorhombic orbital ordered structure similar to the one observed in the stoichiometric LaMnO_3 ³⁹. The second transition at lower temperature is related to the charge ordering of the Mn-ions and is accompanied by the lowering symmetry

to the monoclinic one and the unit cell doubling along the orthorhombic a -axis. We have studied the crystal structure of several compositions of LPCM up to the high temperatures across the transition to the pseudocubic phase.

C. Orbital order-disorder transition

The study the crystal structure of LPCM up to the transition to the pseudocubic phase allowed us to get a wide range of the changes in the crystal structure, which helped to understand the temperature behavior of the crystal structure at low temperature. Figure 7 shows the crystal lattice constants and the isotropic micro-strain parameter ($\delta d_{st}/d$) in the LPCM sample with $y=0.75$. The latent heat at the transition temperature T_{J-T} (insert in Fig. 7) points to the first order phase transition. Above the transition the crystal structure is metrically cubic and the refinement in the profile matching mode in the cubic metrics gives the same quality of the fit (χ^2) with the lattice constant shown by rhombs in Fig. 7a. In addition, the MnO_6 octahedron gets regular above the transition. The structure is thus becoming pseudo-cubic. This has inspired us to search for a possible alternative cubic crystal structure description, similar to the attempt undertaken in³⁹. The diffraction pattern at 800 K is indexed in the cubic cell with $a = 7.76$ Å. The list of possible space groups with their numbers in brackets, which does not contradict the set of observed diffraction peaks contains seven possibilities: $P2_13$ (198), $P4_23m$ (208), $P23$ (195), $Pm\bar{3}$ (200), $P432$ (207), $P\bar{4}32$ (215) and $Pm\bar{3}m$ (221). Our trial structure solutions (carried out with the program FOX⁴⁰) did however fail to find a suitable candidate structure model. As it was actually pointed out in³⁹, the failure could have been predicted by the even earlier studies by Glazer⁴¹, who did not deduce any primitive cubic space group for the structure with lattice constant $2a_p$ for the distorted perovskite which could have originated from the coherent octahedra tilts.

The micro-strain value ($\delta d_{st}/d$) is markedly increased below the transition temperature (Fig. 7b). The lattice constant mismatch in the adjacent crystal domains and/or twins naturally creates the internal micro-strains below the transition T_{J-T} . This is important to note because the phase separation at low temperature depends on the value of the micro-strains, which will be inevitably present in the LPCM system due to this structure transition.

Figure 8 shows the bond lengths between manganese and oxygen atoms in the MnO_6 -octahedra as a function of temperature. Mn-O1 is the bond directed to the oxygen in the

position shifted along y -direction with respect to the Mn-atom. Mn-O21 and Mn-O22 are the bonds to the oxygen atoms located roughly in the (ac) plane. The transition at T_{J-T} is a Jahn-Teller type of transition connected with the lifting up of the e_g orbital degeneracy. The filling of the e_g orbitals $|e_g\rangle = \cos(\theta/2)|z^2\rangle + \sin(\theta/2)|x^2 - y^2\rangle$ can be determined from the value of an angle θ , which is the polar angle in the plane of normal coordinates (Q_2, Q_3) ⁴². The coordinates are given by the distortion of the MnO_6 octahedron $Q_3 = (1/\sqrt{2})(l - s)$, $Q_2 = (2/\sqrt{6})(2m - l - s)$, where s , m , l are the short, medium and long Mn-O bond lengths, respectively. One can see from the Fig. 8 that above T_{J-T} all three bonds are equal, implying that both e_g -orbitals are equally populated. Below the transition two of them remain equal ($m = s$), that gives the angle $\theta = 2\pi/3$. This angle corresponds to the complete filling of the y^2 -orbital or for another choice of axes to equivalent z^2 - or x^2 - orbitals [they are related to each other by $2\pi/3$ rotation in the (Q_3, Q_2) -plane]. In the $Pnma$ structure it corresponds to the antiferrodistorsive type of orbital ordering (OO) schematically shown in the Fig. 8. It is interesting to compare with the case of LaMnO_3 , where below the transition the z^2 -orbital is $\sim 65\%$ filled, while above the transition the angle θ amounted to $\theta \simeq \pi/2$ ($Q_3 = 0$), which also corresponds to the equal filling of the e_g orbitals³⁹. In the later case the Q_2 -type of the octahedron distortions remain in the high-temperature phase due to the interactions between the distortions. In our case the interaction between the Jahn-Teller active Mn^{3+} ions is weakened due to the dilution by 30% of the statistically distributed Mn^{4+} ions and thus the MnO_6 octahedron behaves like a free molecule with equally populated e_g -orbitals. The difference in the in-plane bond lengths Mn-O2 in the OO state at room temperature is an order of magnitude smaller in the case of LPCM (cf. 0.27 Å vs. 0.02 Å). This abrupt decrease in the bond length mismatch as a function of the Mn^{3+} fraction is an additional evidence of the cooperative nature of the Jahn-Teller effect. In the $\text{La}_{0.5}\text{Ca}_{0.5}\text{MnO}_3$ where the ratio of $\text{Mn}^{3+} : \text{Mn}^{4+}$ is “50:50” the MnO_6 -octahedron remains almost regular at room temperature⁴³.

D. Charge order transition

The LPCM system undergoes a transition to the charge ordered state (CO) at $T_{CO} > T_N$ ^{9,15}. The transition is revealed by the appearance of weak superstructure peaks reflecting the doubling of the unit cell along a -axis and the lowering of the symmetry probably to

the monoclinic $P2_1/m$ one similar to the case of $\text{La}_{0.5}\text{Ca}_{0.5}\text{MnO}_3$ ⁴³. However, the deviations from the average $Pnma$ structure are small and do not allow a reliable detection of the charge ordering. Better structure indicators of the CO-transition are the increase in the Mn-O bond lengths mismatch and the appearance of the anisotropic lattice micro-strains in the CO state. One can see (Fig. 8) that below ~ 250 K the two equal Mn-O bond length become different. We believe that this is a manifestation of the charge ordering which is schematically shown as insert in Fig. 8. This type of $\text{Mn}^{3+}/\text{Mn}^{4+}$ and orbital ordering in the (ac) plane is dictated by the Goodenough-Kanamori rules and the low temperature magnetic structure (PCE). In Ref.⁹ there was proposed that in $\text{Pr}_{0.7}\text{Ca}_{0.3}\text{MnO}_3$ the sites shown with the z^2 -type orbital are fully occupied by Mn^{3+} , while those shown by circles are occupied by $\text{Mn}^{3+} : \text{Mn}^{4+}$ with the ratio 40 : 60. Since the structure is described in the average $Pnma$ space group the atom positions are averaged over the symmetry elements of $Pnma$. The orbital ordering in the charge ordered phase would give roughly equal average in-plane Mn-O2 bond length. However, even in an ideal case of CO in $\text{La}_{0.5}\text{Ca}_{0.5}\text{MnO}_3$ the in-plane Mn-O2 bond lengths become different in the CO-phase at low temperature in the $Pnma$ -description⁴³. The in-plane Mn-O2 bond length mismatch in the LPCM is larger apparently due to the larger Mn^{3+} fraction. An evident indicator of the charge ordering is the mismatch of the short Mn-O22 and Mn-O1 bond lengths. In the antiferrodistorsive OO state all the z^2 -orbitals are in the ac -plane, while below the CO-transition the z^2 -orbitals located at “ Mn^{4+} ” sites should be oriented perpendicular to the (ac)-plane to stabilize the ferromagnetic coupling between the neighboring planes along b -axis of the PCE-type antiferromagnetic structure. This is reflected as a decrease in the short Mn-O22 with respect to the Mn-O1 bond below ~ 250 K (Fig. 8). Figure 9 shows the temperature dependences of the bond lengths as a function of Pr-concentration y . One can see that the difference of the Mn-O1 and Mn-O22 bond lengths is drastically decreased near $y = 0.9$, reflecting the suppression of the charge ordering. In the metallic predominantly ferromagnetic state ($y \leq 0.5$) CO is suppressed as well. Another parameter which can be considered as a structure indicator of the CO state is the anisotropic micro-strain $(\delta d_{\text{st}}/d)_{[100]}$ along a -axis, along which the doubling of the unit cell occurs in the CO phase. This implies that the CO/OO is not perfectly homogeneous as in purely “50:50” composition $\text{La}_{0.5}\text{Ca}_{0.5}\text{MnO}_3$ but there is a distribution of domains with different extent of CO thus leading to the dispersion of the lattice constant a . The anisotropic micro-strain is pronouncedly increased on cooling for $y \geq 0.7$, but has a nonzero

value at room temperature 290 K as shown in Fig. 10. A remarkable feature of $(\delta d_{\text{st}}/d)_{[100]}$ is a local minimum around $y_c = 0.9$ pointing to a suppression of the CO concomitantly with the suppression of the AFM and FM ordering as discussed below. The isotropic micro-strain value $(\delta d_{\text{st}}/d)_{\text{iso}}$ (also shown in Fig. 10) doesn't exhibit any peculiarity at y_c ruling out any kind of sample effect.

E. Magnetic state

The temperature dependences of the magnetic Bragg peak intensities $I(T)$ allow accurate determining of the transition temperatures to the AFM and FM states (T_N , T_C). A typical diffraction pattern is shown in Fig. 4, where the tick rows indicate the nuclear and magnetic phases. The magnetic structure consists of AFM pseudo-CE component with Mn-spin directed along b and FM component in (ac) -plane similar to the one reported in^{9,10}. In addition, the Pr-spins also get ferromagnetically ordered parallel to the FM-component of Mn-spins. The refined low temperature magnetic moments are presented in Table I. Figure 11 shows several examples of the temperature dependences of the selected magnetic Bragg peaks $I(T)$. The ^{16}O and ^{18}O samples for each y -concentration were prepared in the same amounts and measured in the identical experimental conditions and thus the integrated intensities shown in Fig. 11 were normalized only to the neutron monitor (number of incoming neutrons). Above 100K the samples with $y \geq 0.7$ are in purely AFM state that is not affected by the oxygen substitution. The Neel temperatures T_N are the same and the whole sample volume is occupied by the AFM phase, as illustrated by Fig. 11b. The ferromagnetic phase is suppressed by the increase in the oxygen mass that is reflected by the splitting of the AFM integrated intensities for the ^{18}O and ^{16}O samples roughly below 100K.

One sees that the AFM transition is very well defined by the abrupt vanishing of the respective Bragg peaks. The ferromagnetic state is destroyed in a more smoother way. Some fraction of the sample volume remains ferromagnetic above the transition as one can see from the smeared shape of the FM Bragg peak intensities $I(T)$ near T_C . To determine the transition temperatures in an unbiased systematic way we performed least-square fits of the experimental $I(T)$ in assumption of the Gaussian distribution of the transition temperatures and a phenomenological power-low function for the spontaneous magnetization:

$$I(T) = I_1 \int_0^\infty \frac{1}{\sqrt{2\pi}\delta T_C} e^{(\tau-T_C)^2/2\delta T_C^2} (1 - (T/\tau)^\alpha)^\beta (1 - H(T - \tau)) d\tau + I_0, \quad (1)$$

where H is a step-like Heaviside function, T_C and δT_C are the mean transition temperature and r.m.s. variance, respectively. I_1 and I_0 are the refinable parameters. For the compositions with $y > 0.5$ the parameters α and β were fixed as indicated in Table I. Otherwise, the fit parameters got unreasonable values. To reduce a number of the refined parameters the experimental $I(T)$ curves for ^{18}O and ^{16}O -samples were processed in one combined fit with the same parameters α , β and I_0 . The results of the fits of the ferromagnetic $I(T)$ to the formula (1) are shown by thick lines in Fig. 11. For comparison, the thin lines for the sample with $y = 0.5$ show the calculated $I(T)$ curves deconvoluted from the Gaussian smearing. The magnetic transition temperatures are summarized in the Table I and in Fig. 12. The Curie temperatures T_C are in reasonable agreement with the ones determined from the magnetic susceptibility data that are also given in the Table I. One can see from the Fig. 12 that the isotope substitution has a large effect on the T_C , whereas the Néel temperature T_N is invariant as one would expect for the double exchange type of FM and the superexchange AFM interactions, respectively.

The AFM phase has been detected at all concentrations, including $y = 0.2$. T_N for the sample with $y = 0.2$ was not determined, because the AF-fraction is very small [the effective AFM moment at $T = 15$ K is $m_A = 0.24(6)\mu_B$] and the temperature scan would require extremely long measurements. For $y \geq 0.7$, the AF ordering precedes appearance of the FM phase with the temperature lowering. The FM phase appears spatially separated, reducing the sample volume occupied by the AFM phase and thus reducing the slope of the $I_{AF}(T)$ roughly below T_C . The sizes of the FM- and AFM-domains are mesoscopically large ($> 10^3$ Å) estimated in the similar way as described in Ref.¹⁰. The same effect of phase separation is present for $y = 0.5$, where $T_C > T_N$ (Fig 11a) implying that there are two characteristic energy scales connected with the ferromagnetism. One (T_C) is given by the double exchange mechanism with the strong dependence on y . The second characteristic temperature is about 130 K where the phase redistribution in favor of the FM state is triggered on.

Figure 12 shows the effective FM $m_F(y)$ and AFM $m_A(y)$ magnetic moments of Mn-ions at base temperature (10-15 K) as a function of y . m_A is the average value of the moments for two sublattices m_{A1} and m_{A2} presented in Table I. The effective moment is

proportional to the product of the real moment and square root of the volume occupied by the ordered phase. Since the crystal structure is well refined in a single phase approximation one cannot determine from a single diffraction measurement whether the magnetic state is a homogeneous one. However, it becomes possible from the analysis of the values of the effective magnetic moments for all the concentrations y for both ^{16}O and ^{18}O -samples. Figure 13 shows $m_A^2(m_F^2)$ for all the samples with the Pr-concentration y as a parameter. The line is a least-square fit to the linear function $m_A^2 = M_A^2(1 - m_F^2/M_F^2)$ for all y except $y = 0.9$ and $y = 1$ with ^{18}O . This linear relation is virtually possible only in assumption of the phase separated state. Otherwise, one would have to suppose quite unreasonable sizes of the magnetic moment as a function of y and the oxygen mass. This linear function assumes that the magnetic moments in the AFM and FM phases keep the constant values $M_A = 2.26(1)\mu_B$, $M_F = 3.57(2)\mu_B$ over the whole phase diagram, but the phase volumes are synchronously redistributed as indicated by top- x and right- y axes of Fig. 13. The size of the FM moment well corresponds to the average spin value of $\text{Mn}^{3+}/\text{Mn}^{4+}$ ions $3.7 \mu_B$, whereas the AFM moment is substantially lower. It can be connected with a “defect” charge ordering that causes a frustration in the magnetic exchange between the neighboring (ac) planes. With the help of the Fig. 13 one can disentangle the effect of the FM/AFM volume redistribution (the points slide along the straight line) and the effect of the suppression of the magnetic ordering (the points lay below the line). The increase in the oxygen mass simply shifts the balance between the phases towards the AFM one for the “metallic” part of the phase diagram ($y \leq 0.8$), similar as the increase in y does, implying that the effect of the isotope substitution is the polaronic narrowing of the bandwidth. The FM phase is metallic and if its volume decreases below the percolation limit $\sim 16\%^4$ then the sample should become an insulator. In the “insulating” part of the diagram ($y \geq 0.9$) the system behavior is very different. Firstly, the ferromagnetic phase is not any more metallic because its fraction, e.g. in the sample with $y = 1$ is far above a percolation threshold corroborating the insulating character of the FMI phase. Secondly, the increase in the oxygen mass suppresses only the FMI phase, both T_C and the effective magnetic moment, leaving the AFM phase fraction intact. One can speculate that the FMI cannot be converted to the AFM phase because it is already insulating and thus the further decrease in the electron transfer integral doesn’t necessarily shift the system towards the AFM state. We suppose that those spins that stop contributing to the FM phase become disordered thus reducing the effective moment.

However we cannot distinguish whether a spatially separated disordered phase is formed or some spins inside the ferromagnetic host get frustrated. The presence of the isotope effect on the FMI is remarkable itself, because it rules out an ordinary superexchange mechanism of FMI. This has been noted in Ref.¹¹ where the isotope effect on T_C was found in insulating $\text{Pr}_{1-x}\text{Ca}_x\text{MnO}_3$, and the genuine FMI state was proposed to appear due to some CO/OO superstructure or density wave giving an energy gap which is much smaller than the Hubbard on-site repulsion.

F. Effect of micro-strains on phase separation

The specific low temperature FM/AFM volume fractions shown in Fig. 13 do not represent themselves universal for LPCM system values that depend only on y . Earlier we studied virtually the same series of samples only with ^{16}O (N-series)¹⁰, but prepared by the different chemical route than the one explained in section II. The phase redistribution process in the N-series samples (Fig. 8 of Ref.¹⁰) triggered at about T_C on cooling goes much “easier” leaving predominantly ($> 90\%$) FM ground state for $y \geq 0.8$, while in the O-series samples the FM fraction is decreased to 73% for $y = 0.8$. The increase in the oxygen mass leads to a complete phase volume redistribution in favor of the AFM phase in the N-series sample with $y = 0.75$ ¹⁵. In the case of the O-series samples, the phase balance is also definitely shifted towards the AFM state (Fig. 13), but none of the ^{18}O -sample shows purely AFM ground state. We have repeated the oxygen treatment and oxygen isotope exchange with the N-series sample in the same way as we did with the samples of the present O-series, including the back exchange and got essentially the same results as in^{3,15}. It is believed that the qualitative difference between the two series originates from smaller grain sizes of the starting reagents in case of the N-series that could give different micro-structure of the sample crystallites. We have undertaken a quantitative micro-structure comparison of two exemplary samples with $y = 0.75$ from each series also using ultra high resolution synchrotron x-ray diffraction (as described in sec. IIIB). Both samples are well refined with the close values of structure parameters. The noticeable difference between the samples from the different series is their micro-structure. The insert of Fig. 4 shows the q -dependence of the reduced peak broadening $\delta d/d$ in the two samples from both series. One can see that the broadening is larger in the O-series sample. The main contribution to $\delta d/d$ comes from the micro-strain

effect amounted to $\delta d_{\text{st}}/d = 0.16\%$ and 0.23% for the N- and O-series sample respectively. Inside the O-series the isotropic micro-strain varies only slightly as shown in the Fig. 10. Thus, the key difference between the two series of the LPCM-samples conditioning their different ground states originates from the different values of $(\delta d_{\text{st}}/d)$ motivating to propose that the phase separation is favored by the micro-strains. The value of the micro-strains can be considered as a quantitative measure of the disorder in the crystal lattice. Many studies of the epitaxial films of manganites have demonstrated that the relative fractions of the FM/AFM phases can be strongly modified by both morphology and strains of the films (e.g.⁴⁴). The strong micro-strain dependence of the phase separated volume fractions in our case suggests that the value of the micro-strains $(\delta d_{\text{st}}/d)$ in the bulk material should also be considered as an additional parameter governing the formation of the phase separated state.

G. Suppression of ordering near $y_c = 0.9$

The Curie temperature T_C is decreased as a function of Pr-concentration y due to the smooth decrease in the Mn-O-Mn bond angle (Fig. 6b), but near the critical concentration $y_c = 0.9$ one can see a local minimum (Fig. 12c), which is unexpected from the behavior of crystal structure parameters. The Néel temperature has a pronounced minimum at y_c , as well. The total volume fraction occupied by both FM and AFM ordered phases decreases by 25% at y_c in comparison with the other samples (Fig. 13). The charge ordering that is concomitant to the antiferromagnetic PCE-type ordering is also suppressed near the critical concentration y_c (section III D).

The suppression of the magnetic transition temperatures and the ordered phase volumes at $y_c = 0.9$ strongly resembles the phase diagram calculated in Ref.¹⁹. The authors of Ref.^{19,20} have shown that introducing of the quenched disorder into an Ising system with two competing ordered states gives an effect of a suppression of the ordering temperatures and mesoscopic phase separation in the vicinity of the bi-critical point. The experimental situation in our case is more complicated. Instead of two phases there are three distinct phases: AFMI phase and concomitant CO phase, FMM metallic phase for $y < y_c$ and FMI insulating phase for $y > y_c$. The phases, which would correspond to the phases separated by the critical point are the FMM metallic from one side and both FMI and AFM insulating phases from another side of MI transition. In the spirit of the above model one would

expect that there is also a phase separation into the FMM and FMI phases near y_c , which are indistinguishable from the present experimental data. The quenched disorder in the LPCM-system is naturally present due the dispersion of the A-cation radius amounting to $\sigma_A \simeq 0.01 \text{ \AA}$ near y_c (this value would nominally correspond to quite large Pr-concentration spread $\Delta y \simeq 0.4$). However, since the radii of the Pr and Ca ions are almost the same the dispersion σ_A limits to zero for $y = 1$, while the phase separated state is still present. The role of the quenched disorder can play the Jahn-Teller strain from Mn^{3+} centres as proposed in Ref.⁴⁵. In addition, the quenched disorder can originate from the chemically inhomogeneous distribution of the A-cations given by the sample preparation procedure.

We cannot exclude also that the lattice distortions and the long-range strain^{18,25} can be the reason for the phase separated state. We note that the suppression effect was not found in a detailed study of similar system $\text{Pr}_{0.65}(\text{Ca}_y\text{Sr}_{1-y})_{0.35}\text{MnO}_3$ ²², where all transition temperatures were continuous through the critical point. The later system has almost the same average A-cation radius but much larger (~ 4 times) variance σ_A , which could be a possible reason of the different behavior. We suppose that to compare the different manganite systems with respect to the effect of the suppression of the ordering near y_c one should also compare the extent of quenched disorder, which can be quantitatively characterized by the value of the isotropic micro-strains.

IV. CONCLUSIONS

The magnetic and crystal structures have been studied in the series of samples $(\text{La}_{1-y}\text{Pr}_y)_{0.7}\text{Ca}_{0.3}\text{MnO}_3$ as a function of the Pr-concentration ($y = 0.2, 0.5, 0.7, 0.75, 0.8, 0.85, 0.9, 0.95, 1.0$) across the metal-insulator (MI) transition around $y_c = 0.9$ and as a function of the oxygen mass (^{16}O , ^{18}O). The ground magnetic state is mesoscopically separated into antiferromagnetic insulating (AFM) and ferromagnetic (FM) phases for all values of y . The ordered magnetic moments of the Mn-ions keep the constant values $M_{AFM} = 2.26(1)\mu_B$, $M_{FM} = 3.57(2)\mu_B$ over the whole phase diagram, whereas the phase fractions are changing as a function of y . The conductivity in the “metallic” part of the phase diagram ($y < y_c$) is metallic because the FM phase is metallic and its fraction is above the percolation threshold. In the “insulating” domain ($y > y_c$) the fraction of the FM phase is significantly above the percolation threshold (e.g. for $y = 1.0$ it amounts to 46%) implying that the FM phase is

insulating for $y > y_c$.

The increase in the oxygen mass has effect on both the values of T_C and the phase fractions. The Curie temperatures of both metallic and insulating FM phases are decreasing in a similar way suggesting that the origin of the ferromagnetism in the insulating state should be connected with a slow electron hopping process similar to the double exchange as discussed in¹¹. The Néel temperature is not affected by the oxygen mass as expected for the AFM superexchange. The increase in the oxygen mass always suppress the FM phase fraction. However, the effect is different for the metallic and insulating FM phase. For $y < y_c$, the oxygen substitution acts similar to the increase in y , namely the FM phase volume fraction is decreased by the same amount as the AFM volume fraction is increased. For $y \geq y_c$ the ferromagnetic insulating phase is suppressed but the AFM phase is not changed at all. Thus, the narrowing of the bandwidth due to the decrease in the A-cation radius and the polaronic narrowing act very differently in the “insulating” part of the phase diagram.

The ratio between the AFM and FM phase fractions is not uniquely a function of the effective bandwidth given by y and the oxygen mass, but is also affected by the value of internal micro-strains that favor the formation of the phase separated state. We propose that the value of the micro-strains can be used as a universal quantity characterizing the extent of the quenched disorder, which can have different origins in the manganites.

The phase diagram of $(\text{La}_{1-y}\text{Pr}_y)_{0.7}\text{Ca}_{0.3}\text{MnO}_3$ has a critical concentration at $y_c = 0.9$, where both Néel T_N and Curie T_C transition temperatures, the ordered phase volumes as well as the charge ordering concomitant to the AFM phase are suppressed. This finding together with the presence of the phase separated state strongly support the theoretical study of the competition between two ordered states in the presence of quenched disorder^{19,20}, implying that the quenched disorder plays a key role in the formation of the phase inhomogeneous state in manganites.

Acknowledgements

This study was partially performed at Swiss neutron spallation SINQ and Swiss light source SLS of Paul Scherrer Institute PSI (Villigen, PSI). We acknowledge A. Kaul, O. Gorbunenko and N. Babushkina for granting us the sample LPCM75 we used in our previous

study^{10,15,29}, L. Keller for the help in neutron diffraction measurements. We thank V. Kabanov for the helpful discussions. The study was supported by the RFBR (grant N06-02-16032).

-
- ¹ G. M. Zhao, K. Conder, H. Keller, and K. A. Muller, *Nature* **381**, 676 (1996).
 - ² G. M. Zhao, H. Keller, J. Hofer, A. Shengelaya, and K. A. Muller, *Solid State Comm.* **104**, 57 (1997).
 - ³ N. A. Babushkina, L. M. Belova, O. Y. Gorbenko, A. R. Kaul, A. A. Bosak, V. I. Ozhogin, and K. I. Kugel, *Nature* **391**, 159 (1998).
 - ⁴ L. P. Gor'kov and V. Z. Kresin, *Phys. Rep.* **400**, 149 (2004).
 - ⁵ H. Y. Hwang, S. W. Cheong, P. G. Radaelli, M. Marezio, and B. Batlogg, *Phys. Rev. Lett.* **75**, 914 (1995).
 - ⁶ N. A. Babushkina, L. M. Belova, A. N. Taldenkov, E. A. Chistotina, D. I. Khomskii, K. I. Kugel, O. Y. Gorbenko, and A. R. Kaul, *J. Phys.-Cond. Matt* **11**, 5865 (1999).
 - ⁷ E. O. Wollan and W. C. Koehler, *Phys. Rev.* **100**, 545 (1955).
 - ⁸ Q. Huang, A. Santoro, J. W. Lynn, R. W. Erwin, J. A. Borchers, J. L. Peng, K. Ghosh, and R. L. Greene, *Phys. Rev. B* **58**, 2684 (1998).
 - ⁹ D. E. Cox, P. G. Radaelli, M. Marezio, and S. W. Cheong, *Phys. Rev. B* **57**, 3305 (1998).
 - ¹⁰ A. M. Balagurov, V. Y. Pomjakushin, D. V. Sheptyakov, V. L. Aksenov, P. Fischer, L. Keller, O. Y. Gorbenko, A. R. Kaul, and N. A. Babushkina, *Phys. Rev. B* **64**, 024420 (2001).
 - ¹¹ L. M. Fisher, A. V. Kalinov, I. F. Voloshin, N. A. Babushkina, K. I. Kugel, and D. I. Khomskii, *Phys. Rev. B* **68**, 174403 (2003).
 - ¹² G. Papavassiliou, M. Pissas, M. Belesi, M. Fardis, J. Dolinsek, C. Dimitropoulos, and J. P. Ansermet, *Phys. Rev. Lett.* **91**, 147205 (2003).
 - ¹³ R. Kajimoto, H. Mochizuki, H. Yoshizawa, S. Okamoto, and S. Ishihara, *Phys. Rev. B* **69**, 054433 (2004).
 - ¹⁴ M. Pissas, I. Margiolaki, G. Papavassiliou, D. Stamopoulos, and D. Argyriou, *Phys. Rev. B* **72**, 064425 (2005).
 - ¹⁵ A. M. Balagurov, V. Y. Pomjakushin, D. V. Sheptyakov, V. L. Aksenov, N. A. Babushkina, L. M. Belova, A. H. Taldenkov, A. V. Inyushkin, P. Fischer, M. Gutmann, et al., *Phys. Rev. B*

- 60**, 383 (1999).
- ¹⁶ M. Tokunaga, Y. Tokunaga, and T. Tamegai, Phys. Rev. Lett. **93**, 037203 (2004).
 - ¹⁷ M. Uehara, S. Mori, C. H. Chen, and S. W. Cheong, Nature **399**, 560 (1999).
 - ¹⁸ P. Littlewood, Nature **399**, 529 (1999).
 - ¹⁹ J. Burgy, M. Mayr, V. Martin-Mayor, A. Moreo, and E. Dagotto, Phys. Rev. Lett. **87**, 277202 (2001).
 - ²⁰ J. Burgy, A. Moreo, and E. Dagotto, Phys. Rev. Lett. **92**, 097202 (2004).
 - ²¹ J. L. Alonso, L. A. Fernandez, F. Guinea, V. Laliena, and V. Martin-Mayor, Phys. Rev. B **66**, 104430 (2002).
 - ²² G. R. Blake, L. Chapon, P. G. Radaelli, D. N. Argyriou, M. J. Gutmann, and J. F. Mitchell, Phys. Rev. B **66**, 144412 (2002).
 - ²³ D. Akahoshi, M. Uchida, Y. Tomioka, T. Arima, Y. Matsui, and Y. Tokura, Phys. Rev. Lett. **90**, 177203 (2003).
 - ²⁴ J. M. De Teresa, P. A. Algarabel, C. Ritter, J. Blasco, M. R. Ibarra, L. Morellon, J. I. Espeso, and J. C. Gómez-Sal, Phys. Rev. Lett. **94**, 207205 (2005).
 - ²⁵ K. H. Ahn, T. Lookman, and A. R. Bishop, Nature (London) **428**, 401 (2004).
 - ²⁶ V. Podzorov, B. G. Kim, V. Kiryukhin, M. E. Gershenson, and S. W. Cheong, Phys. Rev. B **64**, 140406(R) (2001).
 - ²⁷ P. A. Sharma, S. B. Kim, T. Y. Koo, S. Guha, and S. W. Cheong, Phys. Rev. B **71**, 224416 (2005).
 - ²⁸ K. Conder, G. M. Zhao, and R. Khasanov, Phys. Rev. B **66**, 212409 (2002).
 - ²⁹ A. M. Balagurov, V. Y. Pomjakushin, D. V. Sheptyakov, V. L. Aksenov, N. A. Babushkina, L. M. Belova, O. Y. Gorbenko, and A. R. Kaul, Eur. Phys. J. B **19**, 215 (2001).
 - ³⁰ P. Fischer, G. Frey, M. Koch, M. Koennecke, V. Pomjakushin, J. Schefer, R. Thut, N. Schlumpf, R. Buerge, U. Greuter, et al., Physica B **276-278**, 146 (2000).
 - ³¹ P. Fischer, L. Keller, J. Schefer, and J. Kohlbrecher, Neutron News **11**, 19 (2000).
 - ³² J. Rodriguez-Carvajal, Physica B **192**, 55 (1993).
 - ³³ J. P. Franck, I. Isaac, G. Zhang, J. E. Gordon, C. Marcenat, R. Lortz, C. Meingast, F. Bouquet, R. A. Fisher, and N. E. Phillips, Journal of Superconductivity **15**, 571 (2002).
 - ³⁴ J. M. De Teresa, M. R. Ibarra, P. A. Algarabel, C. Ritter, C. Marquina, J. Blasco, J. Garcia, A. D. Moral, and Z. Arnold, Nature **386**, 256 (1997).

- ³⁵ A. M. Balagurov, I. A. Bobrikov, V. Y. Pomyakushin, D. V. Sheptyakov, N. A. Babushkina, O. Y. Gorbenko, M. S. Kartavtseva, and A. R. Kaul', JETP Lett. **82**, 594 (2005).
- ³⁶ S. W. Lovesey, *Theory of neutron Scattering from Condensed matter* (Oxford Univ. Press, 1987), vol. 1, p. 112.
- ³⁷ P. Thompson, D. E. Cox, and J. B. Hastings, J. Appl. Cryst. **20**, 79 (1987).
- ³⁸ P. W. Stephens, J. Appl. Cryst. **32**, 281 (1999).
- ³⁹ J. Rodriguez-Carvajal, M. Hennion, F. Moussa, A. H. Moudden, L. Pinsard, and A. Revcolevschi, Phys. Rev. B **57**, R3189 (1998).
- ⁴⁰ V. Favre-Nicolin and R. Cerny, Journal of Applied Crystallography **35**, 734 (2002).
- ⁴¹ A. M. Glazer, Acta Crystallographica A **31**, 756 (1975).
- ⁴² J. Kanamori, J. Appl. Phys. **31**, S14 (1960).
- ⁴³ P. G. Radaelli, D. E. Cox, M. Marezio, and S. W. Cheong, Phys. Rev. B **55**, 3015 (1997).
- ⁴⁴ T. Wu, S. B. Ogale, S. R. Shinde, A. Biswas, T. Polletto, R. L. Greene, T. Venkatesan, and A. J. Millis, J. Appl. Phys. **93**, 5507 (2003).
- ⁴⁵ D. N. Argyriou, U. Ruett, C. P. Adams, J. W. Lynn, and J. F. Mitchell, New Journal of Physics **6**, 195 (2004).

TABLE I: The effective ferro- and antiferromagnetic moments at $T \leq 15$ K and the Néel T_N and Curie T_C transition temperatures in the $(\text{La}_{1-y}\text{Pr}_y)_{0.7}\text{Ca}_{0.3}\text{MnO}_3$. T_C were determined from the fits of neutron diffraction intensities to formula (1) (ND) and by the inflection point of magnetic susceptibility (χ). δT_C is r.m.s. variance of the Gaussian distribution of the transition temperatures. See the text for details. The values of the moments are given in μ_B . The Mn-magnetic moments of the pseudo-CE AFM structure are m_{A1} and m_{A2} for the propagation vectors $k_1=[0\ 0\ 1/2]$ and $k_2=[1/2\ 0\ 1/2]$, respectively. m_F is the FM moment of Mn-ion. m_{Pr} shows the magnetic moment of Pr-ion.

Oxygen	y	T_N	T_C ND; χ	δT_C	m_{A1}	m_{A2}	m_F	m_{Pr}
^{16}O	0.2	-	240.3(1); 236(2)	0^a	0.06(18)	0.23(5)	3.57(2)	0^a
^{18}O	0.2	-	221.4(4); 224(2)	0^a	0.23(8)	0.26(7)	3.46(3)	0^a
^{16}O	0.5	160(3)	183(2); 180(2)	14(2)	0.36(5)	0.29(7)	3.53(2)	0^a
^{18}O	0.5	160(3)	164(2); 155(2)	19(2)	0.95(3)	0.91(4)	3.25(2)	0^a
$^{16}\text{O}^b$	0.7	163(3)	138(2); 122(2)	30(3)	1.11(5)	1.03(4)	3.22(2)	0.48(2)
$^{18}\text{O}^b$	0.7	163(3)	122(2); 116(2)	29(3)	1.41(4)	1.33(3)	2.79(2)	0.64(3)
^{16}O	0.75	-	- ; 122(2)	-	1.03(5)	0.97(5)	3.21(2)	0.52(2)
^{18}O	0.75	-	- ; 116(2)	-	1.34(4)	1.29(3)	2.72(2)	0.63(3)
$^{16}\text{O}^b$	0.8	153(3)	120(1); 120(2)	23(2)	1.30(4)	1.28(3)	3.03(2)	0.49(2)
$^{18}\text{O}^b$	0.8	153(3)	107(2); 114(2)	16(3)	1.63(3)	1.66(2)	2.38(2)	0.57(3)
$^{16}\text{O}^b$	0.85	150(3)	100(3); 116(2)	35(4)	1.82(3)	1.79(3)	2.34(4)	0.35(6)
$^{16}\text{O}^b$	0.9	135(3)	90(2); 99(2)	21(3)	1.63(3)	1.75(2)	1.58(2)	0.39(3)
$^{18}\text{O}^b$	0.9	135(3)	86(3); 94(2)	17(4)	1.62(3)	1.74(2)	1.19(3)	0.63(4)
$^{16}\text{O}^b$	0.95	145(3)	99.0(9); 117(2)	17(1)	1.96(3)	1.93(4)	1.94(5)	0.39(7)
$^{16}\text{O}^b$	1.0	150(3)	104.1(8); 120(2)	14(2)	1.63(3)	1.61(3)	2.40(2)	0.53(2)
$^{18}\text{O}^b$	1.0	150(3)	98(1); 115(2)	15(2)	1.62(3)	1.60(3)	2.12(2)	0.61(2)

^afixed

^b_a=2 and _b=0.66 are fixed in formula (1)

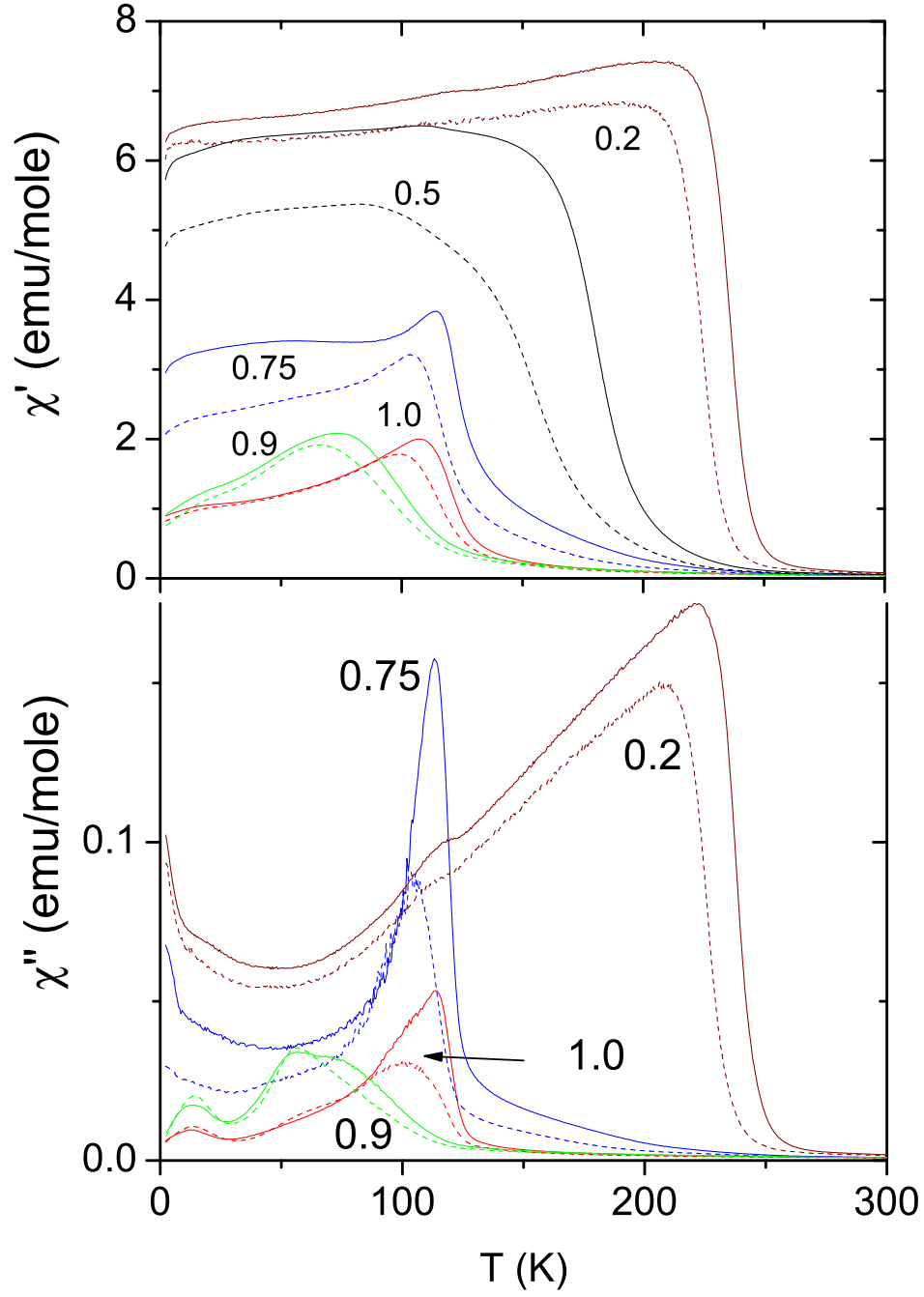


FIG. 1: (color online) Real χ' and imaginary χ'' parts of the *ac* magnetic susceptibility are shown as a function of temperature for several samples with the Pr-content y indicated in the plots. ^{16}O and ^{18}O -samples are shown by solid and dashed lines respectively. χ'' for $y = 0.5$ (which is similar to one for $y = 0.2$) is not shown to avoid plot overload.

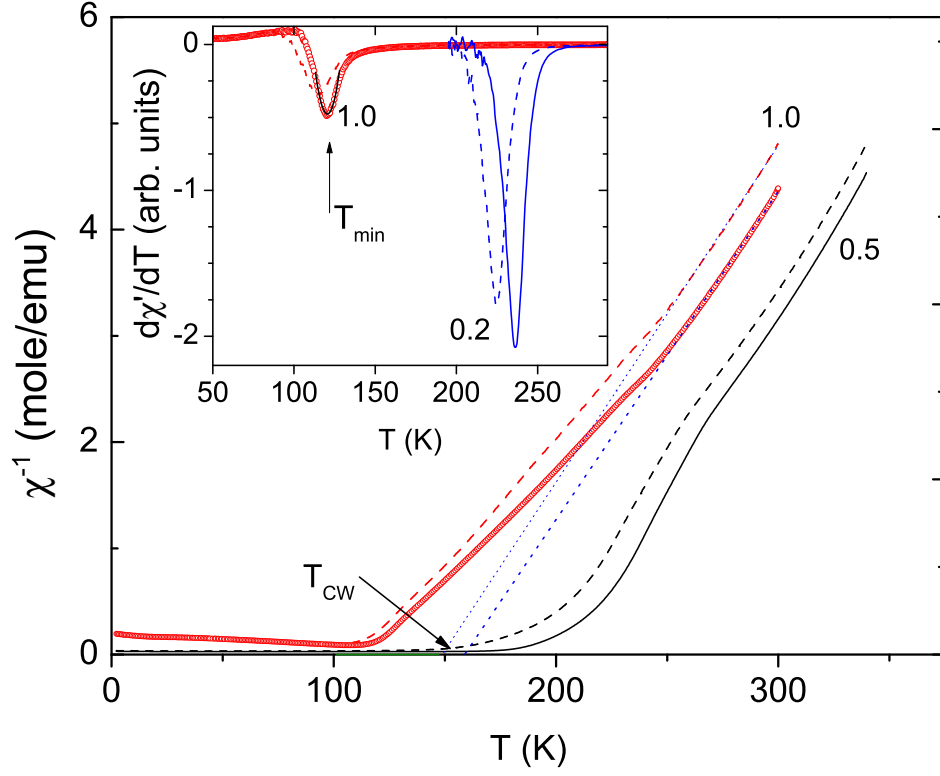


FIG. 2: (color online) χ'^{-1} as a function of temperature for the Pr-content y indicated in the plots. The dotted lines show the fits of high temperature part of χ' to the Curie-Weiss law. The refined Curie temperatures T_{CW} are indicated. The insert shows two examples of the first derivative $d\chi'/dT$ as a function of temperature. ^{16}O and ^{18}O -samples are shown by solid and dashed lines, respectively except for the $y=1.0$ (^{16}O) sample, which is shown by circles. The solid line in the insert for this sample shows example of the parabolic fit. The refined temperature of the minimum is indicated in the insert.

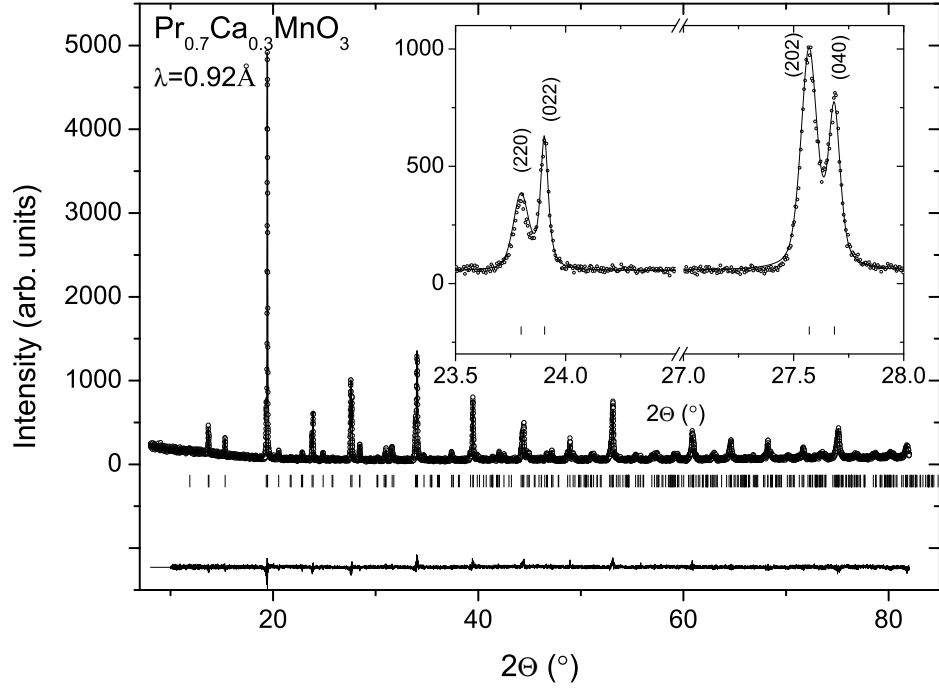


FIG. 3: An example of the Rietveld refinement pattern and difference plot of x-ray synchrotron diffraction data (MSP/SLS, PSI, $\lambda = 0.92 \text{ \AA}$) for the sample with $y=1.0$ at room temperature. The insert illustrates anisotropic line broadening along a -axis.

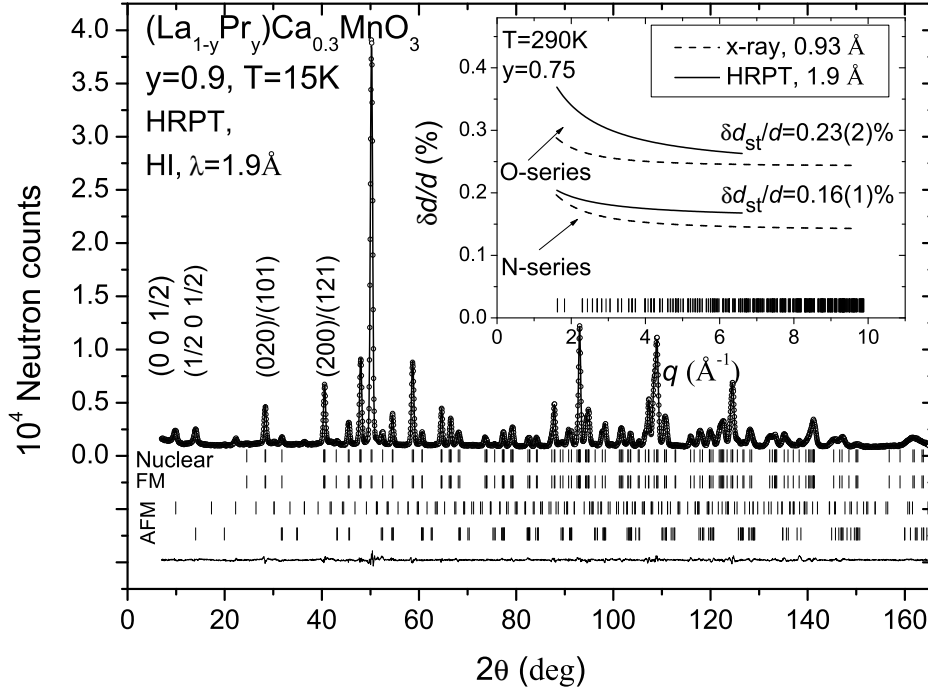


FIG. 4: An example of the Rietveld refinement pattern and difference plot of the neutron diffraction data for the sample with $y = 0.9$ at $T=15\text{K}$. The most intensive magnetic peaks are indicated by Miller indices. The insert illustrates the reduced FWHM of the Bragg peak broadening ($\delta d/d$) as a function of q for two samples with $y = 0.75$ from O- and N-series at room temperature measured by neutron and x-ray synchrotron diffraction. ($\delta d/d$) was calculated from the refined FWHM-width of the Bragg peaks after deconvoluted with the instrument resolution function. $\delta d_{st}/d$ are the refined isotropic micro-strain value. See the text for details.

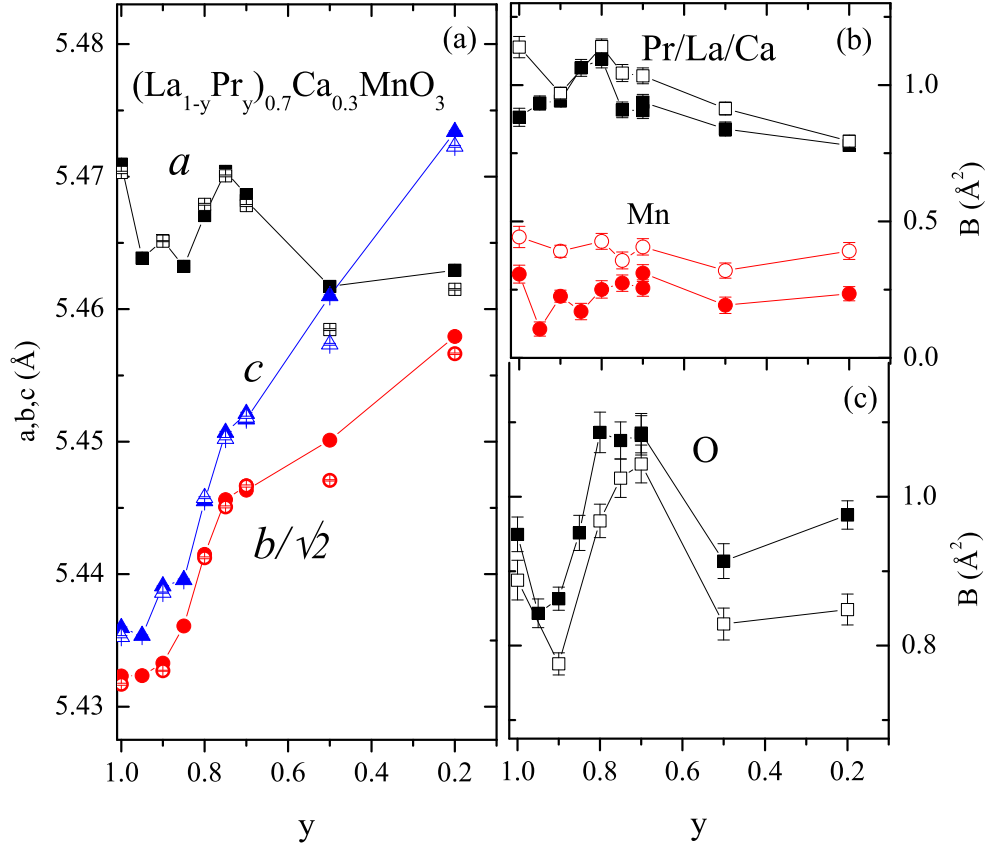


FIG. 5: (color online) (a) The lattice constants (sp. gr. $Pnma$) and (b,c) isotropic thermal parameters at room temperature $T = 290$ K. ^{16}O and ^{18}O -samples are shown by closed and open symbols respectively.

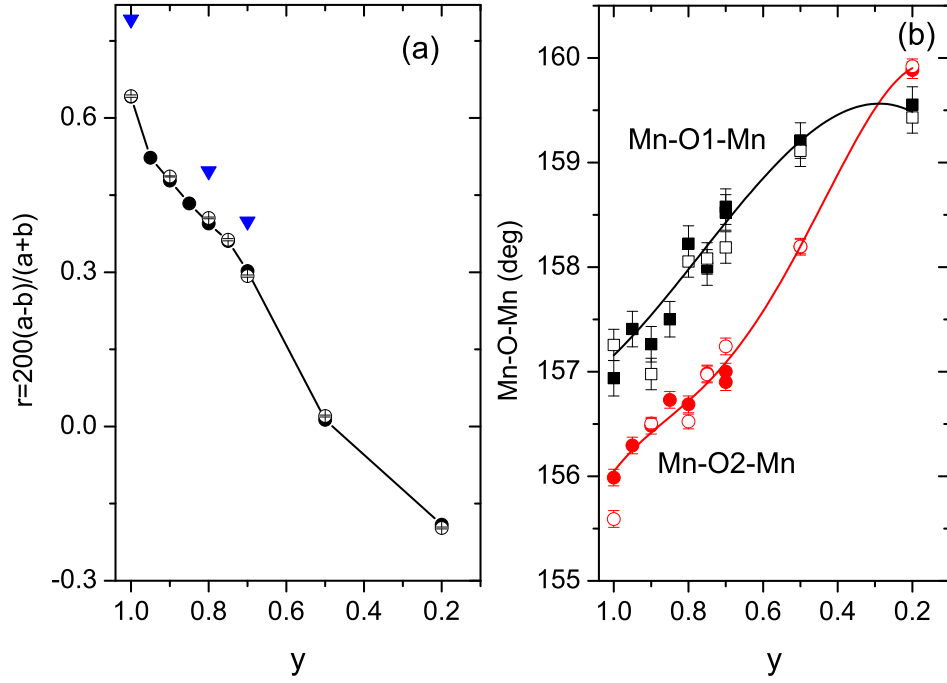


FIG. 6: (color online) (a) The orthorhombic strain r and (b) Mn-O-Mn bond angles as a function of Pr concentration (sp. gr. $Pnma$) at room temperature $T = 290$ K. ^{16}O and ^{18}O -samples are shown by closed and open symbols respectively. The triangles in (a) show the orthorhombic strain in the “as prepared” samples for comparison. The lines are guides for the eyes.

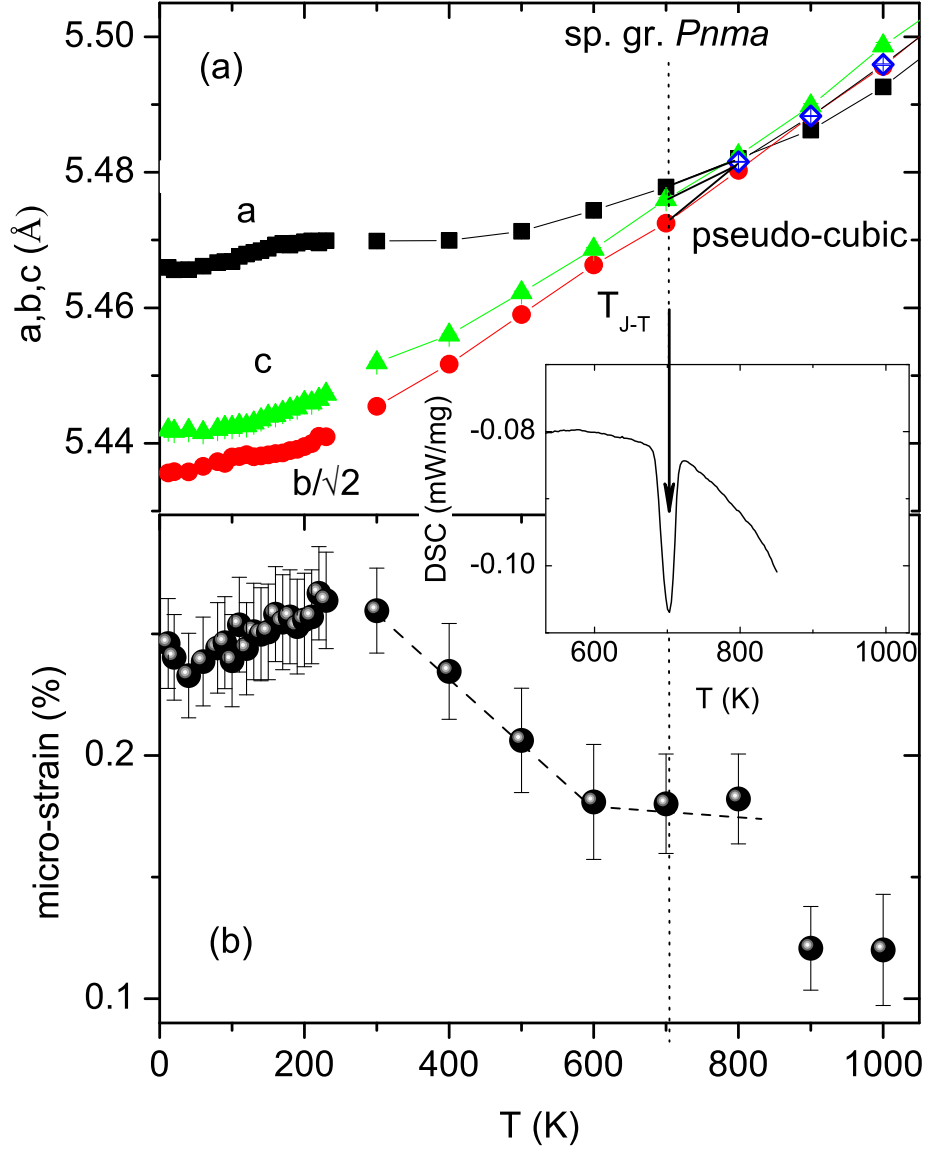


FIG. 7: (color online) (a) Lattice constants and (b) isotropic micro-strains as a function of temperature in the $(\text{La}_{1-y}\text{Pr}_y)_{0.7}\text{Ca}_{0.3}\text{MnO}_3$ ($y=0.75$). The insert shows the differential scanning calorimetry signal with the same x-axis. The minimum indicates the presence of the latent heat of the first order phase transition at the temperature T_{J-T} .

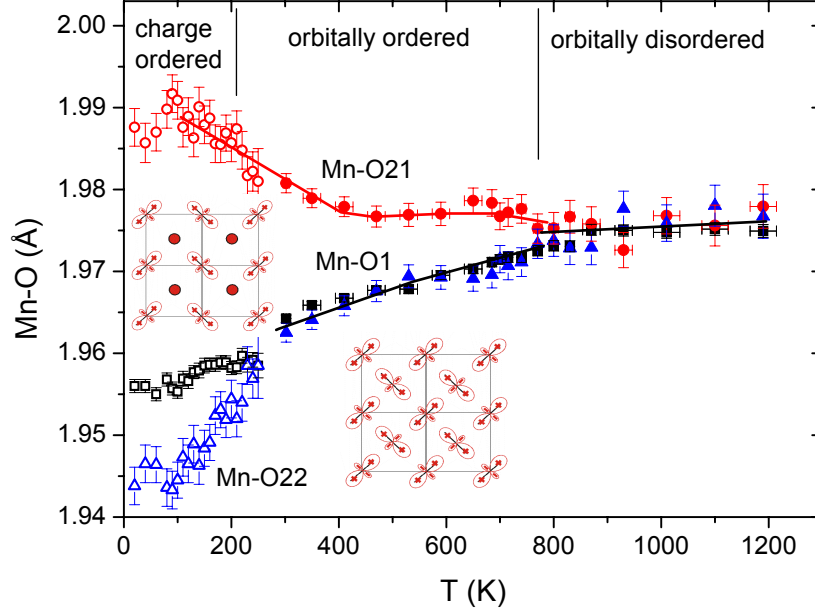


FIG. 8: (color online) Bond length Mn-O1 and Mn-O2 being approximately along and perpendicular b -axis, respectively as a function of temperature in $(\text{La}_{1-y}\text{Pr}_y)_{0.7}\text{Ca}_{0.3}\text{MnO}_3$ for $y=0.7$. The structure undergoes a change from the orbitally disordered pseudocubic phase to the antiferrodistortive type of orbital ordering (OO) below 800K and to the charge ordered (CO) state at lower temperatures. The sketches of the z^2 -type Mn-orbitals in the (ac) plane are shown in the inserts. In the OO phase each Mn-site is statistically occupied by Mn^{3+} and Mn^{4+} . In the CO-phase the fully occupied Mn^{3+} -sites are shown with z^2 -type orbitals, while the sites occupied by both Mn^{4+} and Mn^{3+} are indicated by the circles. See the text for the details.

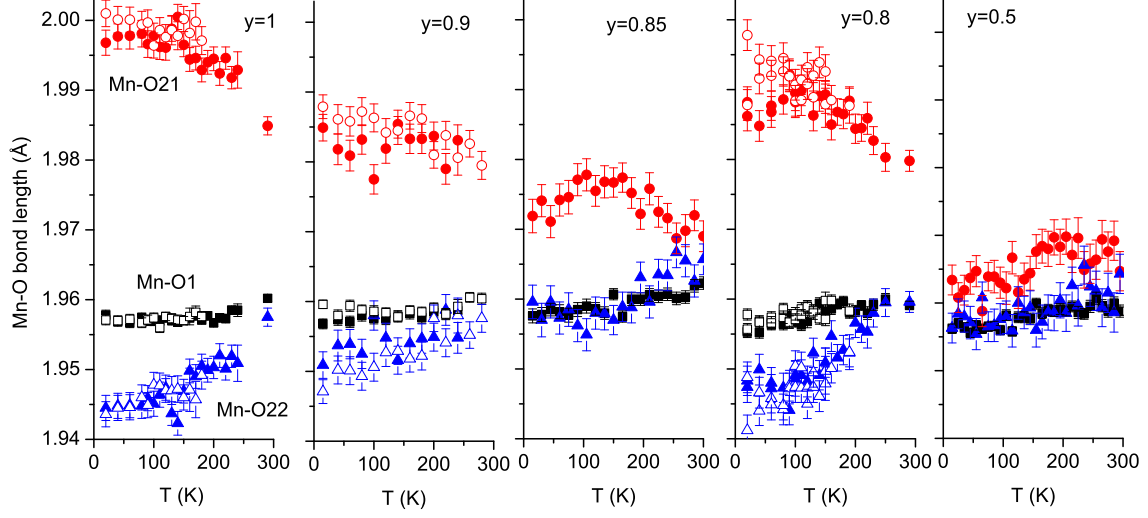


FIG. 9: (color online) Bond length as a function of temperature in $(\text{La}_{1-y}\text{Pr}_y)_{0.7}\text{Ca}_{0.3}\text{MnO}_3$ for the Pr concentration $y=1.0, 0.9, 0.85, 0.8, 0.5$. The bond lengths for the sample with $y=0.7$, are similar to ones for the $y=0.8$ and are shown in Fig. 8. ^{16}O and ^{18}O -samples are shown by closed and open symbols respectively.

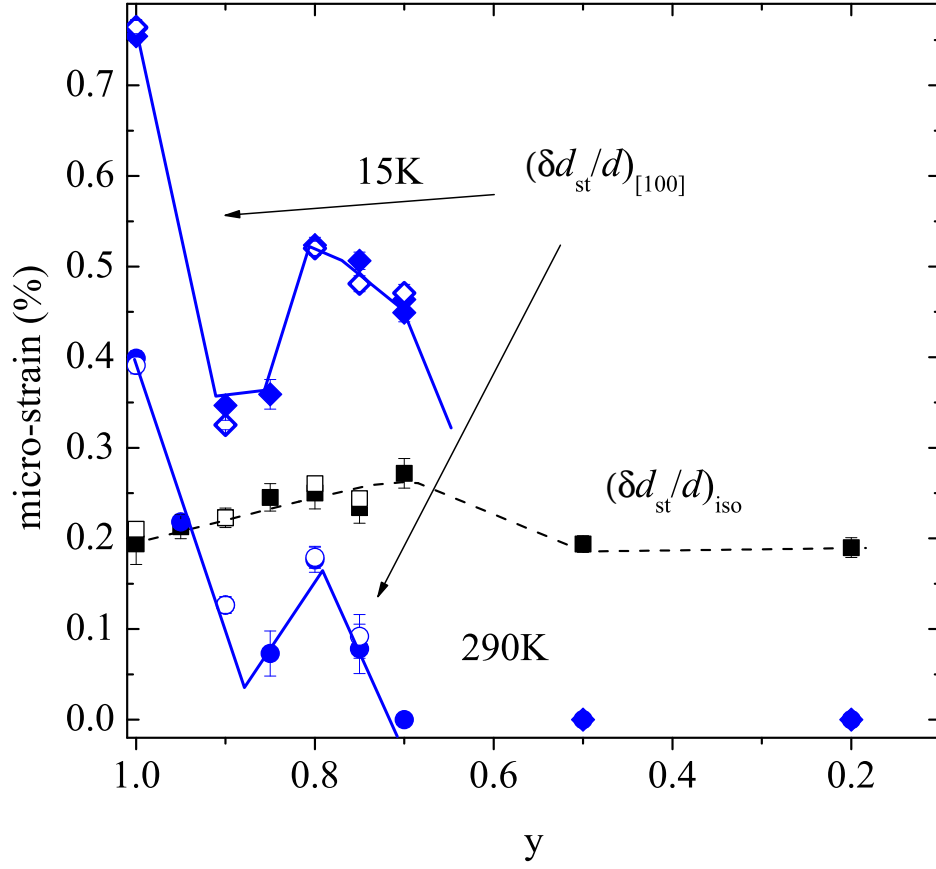


FIG. 10: (color online) (a) The lattice micro-strains as a function of Pr concentration (sp. gr. $Pnma$) at $T = 290$ K. The anisotropic micro-strain $(\delta d_{st}/d)_{[100]}$ is also shown for $T=15$ K. ^{16}O and ^{18}O -samples are shown by closed and open symbols respectively.

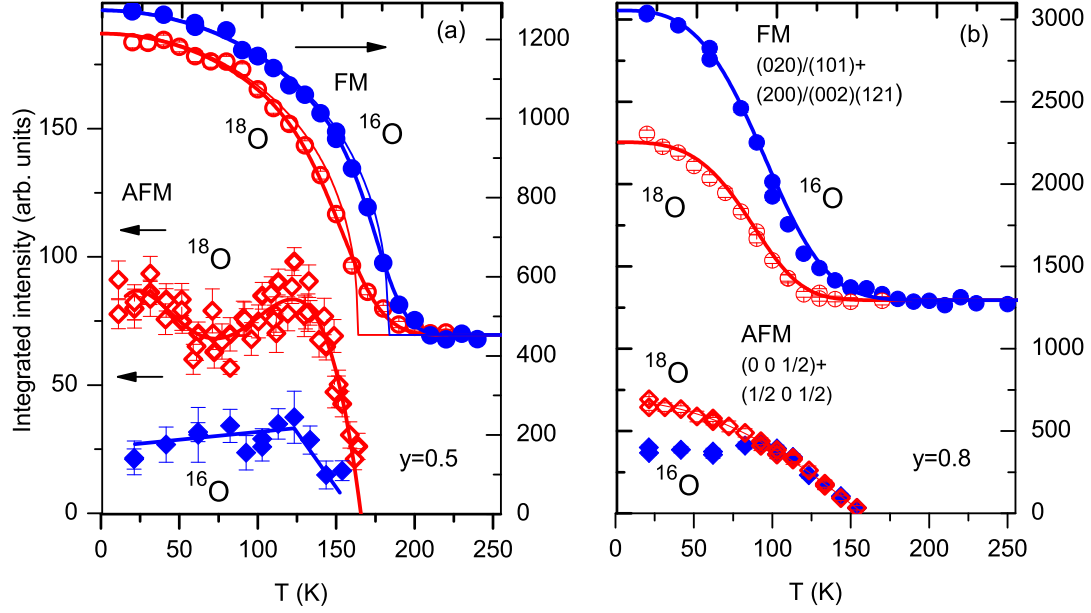


FIG. 11: (color online) Temperature dependences of the integrated intensities of the selected magnetic diffraction peaks indicated in the Fig. 4 in the samples with (a) $y = 0.5$ and (b) $y = 0.8$. The data were collected on heating. ^{16}O and ^{18}O -samples are shown by closed and open symbols respectively. The lines for the AFM intensities are guides to the eye. For the FM ones the lines are fits to the formula described in the text.

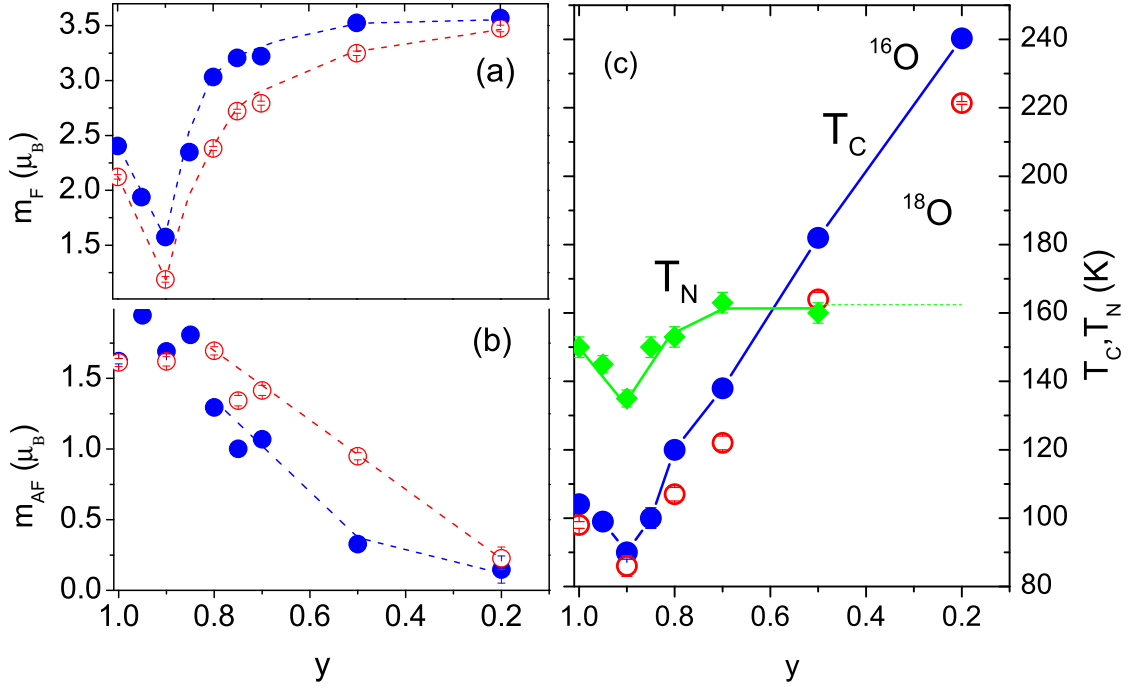


FIG. 12: (color online) Effective (a) ferro- m_F and (b) antiferromagnetic moments m_{AF} at $T=15$ K, (c) Néel T_N and Curie T_C transition temperatures determined from the ND data as a function of y in $(\text{La}_{1-y}\text{Pr}_y)_{0.7}\text{Ca}_{0.3}\text{MnO}_3$. The lines are guides for the eyes. ^{16}O and ^{18}O -samples are shown by closed and open symbols respectively. Néel temperatures for the samples with different oxygen mass are the same.

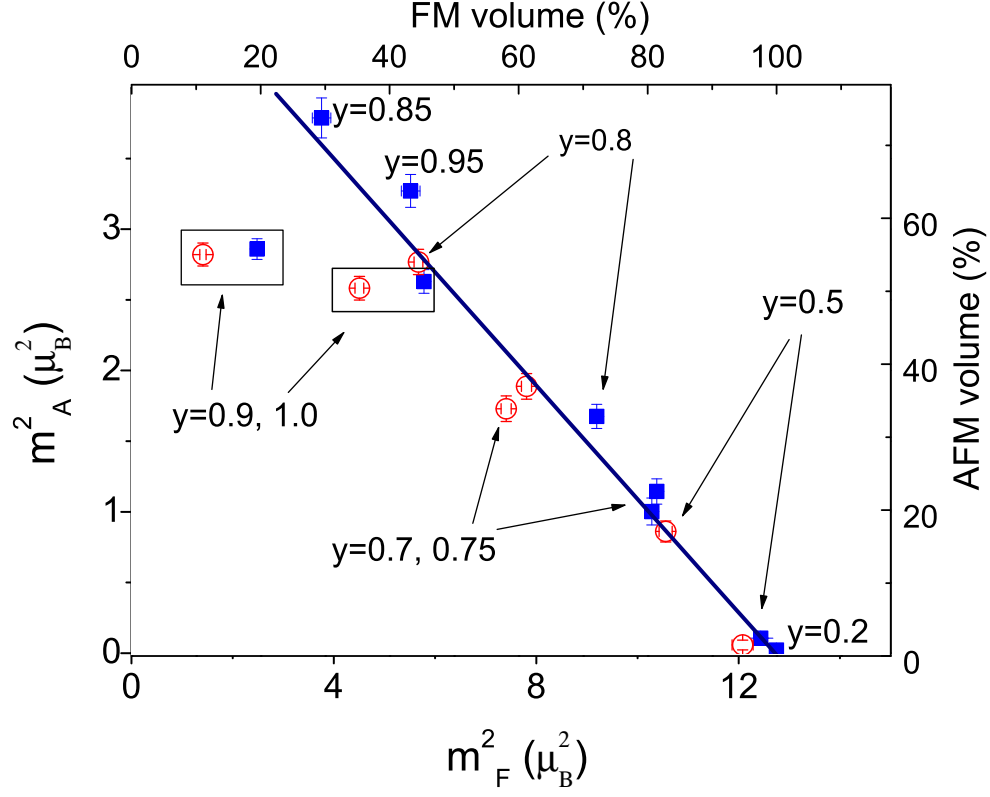


FIG. 13: (color online) Effective antiferromagnetic m_A^2 as a function of the effective ferromagnetic moment m_F^2 for all the samples with y as a parameter indicated for each point. The top- x and right- y axes show respective phase fractions. The line is a linear fit, $y=0.9$ and $y=1.0$ (^{18}O) are excluded from the fit. The closed and open symbols represent the ^{16}O and ^{18}O samples, respectively.